Supporting Information

Robust ditopic enaminone- and hydrazone-linked amine-functionalized porous organic cage for effective permanganate capture and conversion

Jiajia Sheng,[a,b,d] Yanan Guo,[a,d] Guoshi Zhang,[b] Wenjing Wang,[a,c] Kongzhao Su,[b,c,*] and Daqiang Yuan[b,c,*]

† College of Chemistry, Fuzhou University, Fuzhou, 350116, China

[a] *College of Chemistry and Materials Science, Fujian Normal University, Fuzhou, 350007, China*

[b] *State Key Lab of Structure Chemistry, Fujian Institute of Research on the Structure of Matter, Chinese Academy of Sciences, Fuzhou, 350002, China*

[c] *University of the Chinese Academy of Sciences, Beijing, 100049, China*

[d] *Fujian College, University of Chinese Academy of Sciences*

E-mail: skz@fjirsm.ac.cn and ydq@fjirsm.ac.cn

Section S1. General Materials and Measurements

Tetraformylcalix[4]resorcinarene (C4RACHO) was synthesized according to a reported literature procedure[1], All other commercially available reagents were used as received without further purification. Fourier transform infrared (FT-IR) spectra were acquired on a Vertex 750 spectrometer using the KBr pellet method, with measurements recorded from 4000 to 500 cm^{-1}. Thermogravimetric analysis (TGA) was performed using an STA 449F3 thermal analyzer. Samples were heated from 30 to 800 °C under a nitrogen atmosphere at a defined heating rate of 10.0K/min.

Scanning electron microscopy (SEM) and energy-dispersive X-ray spectroscopy (EDS) were conducted on a SU8010 microscope. Ultraviolet-visible (UV-vis) absorption spectra were recorded at ambient temperature on a PerkinElmer Lambda 365 spectrophotometer. Matrix-assisted laser desorption/ionization time-of-flight mass spectrometry (MALDI-TOF-MS) was performed on a Bruker ultrafleXtreme instrument. Powder X-ray diffraction (PXRD) patterns were collected on a Rigaku Mini 600 diffractometer (Cu Kα radiation, λ = 1.54 Å). PXRD simulations were performed using the Mercury software package (single crystal data and diffraction crystal module), available free of charge at http://www.ccdc.cam.ac.uk/products/mercury/. Gas adsorption-desorption measurements were carried out on a fully automated volumetric adsorption instrument (Micromeritics ASAP 2020). The N_2, H_2, and CO_2 adsorption-desorption isotherms of the adsorbent were measured using a Micromeritics ASAP 2020 surface area and porosity analyzer at 77 K, 77 K, and 298 K, respectively. Pore size distribution data were calculated from the N_2 adsorption isotherm at liquid nitrogen temperature based on the DFT model (assuming cylindrical pore geometry) implemented in the Micromeritics ASAP 2020 software package. Pore volume and micropore volume were calculated using the built-in software of the ASAP 2020 physisorption analyzer. Prior to gas adsorption measurements, the POC materials were degassed at 393 K for 10 hours to obtain activated samples.

Section S2. Synthetic Procedures and Characterizations

Synthesis of DPOC-1: Tetraformyl-functionalized calix[4]resorcinarene (C4RACHO) (0.025 mmol, 20.5 mg) and 3,4-diaminobenzhydrazide (0.05 mmol, 8.3 mg) were placed in a 10 mL vial. DMF (2.5 mL) and methanol (1.5 mL) were added sequentially. The reaction mixture was heated at 65°C in an oven for 48 hours. during which red strip-shaped crystals were formed. After removing the glass vial from the oven and allowing it to cool to room temperature for about an hour without stirring, red strip-shaped crystals were then separated by filtration and washed three times with methanol. The separated crystals were further immersed and exchanged 6 times every 24 hours in methanol before activating at 100 °C under a high vacuum for 12 hours to afforded **DPOC-1** with yield of 77%. MALDI-TOF-MS: $[M-H]^{-}$·calcd. for **DPOC-1** ($C_{186}H_{204}N_{24}O_{30}$) is 3254.751; found 3254.254.

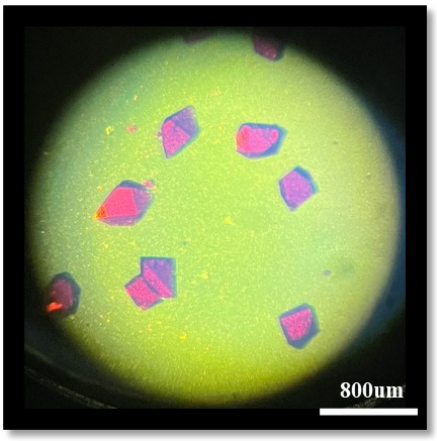

Figure S1. Optical microscopy images of crystalline samples for **DPOC-1**.

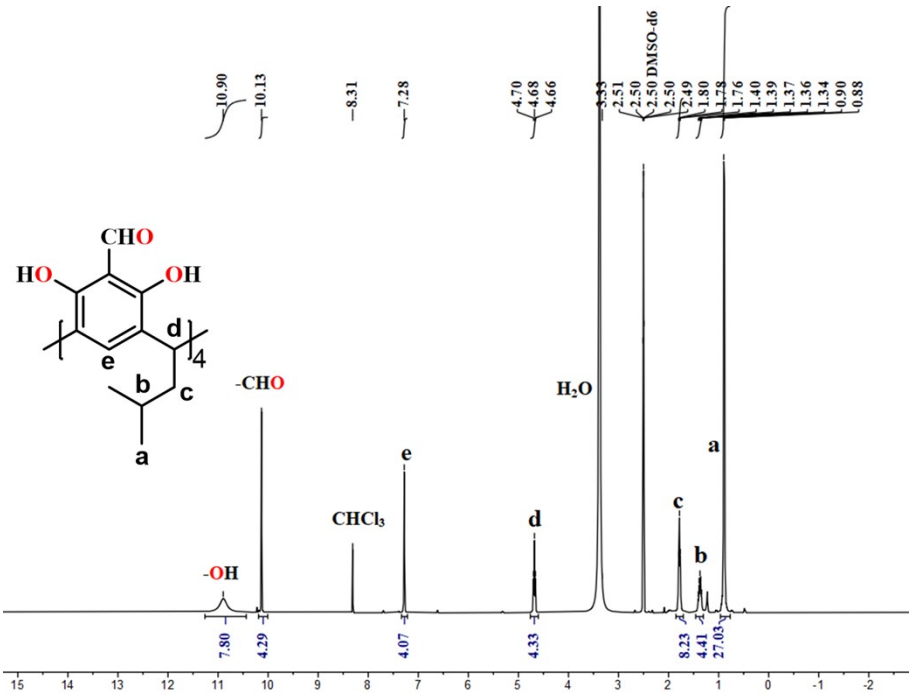

Figure S2. ^{1}H NMR spectrum of **C4RACHO.**

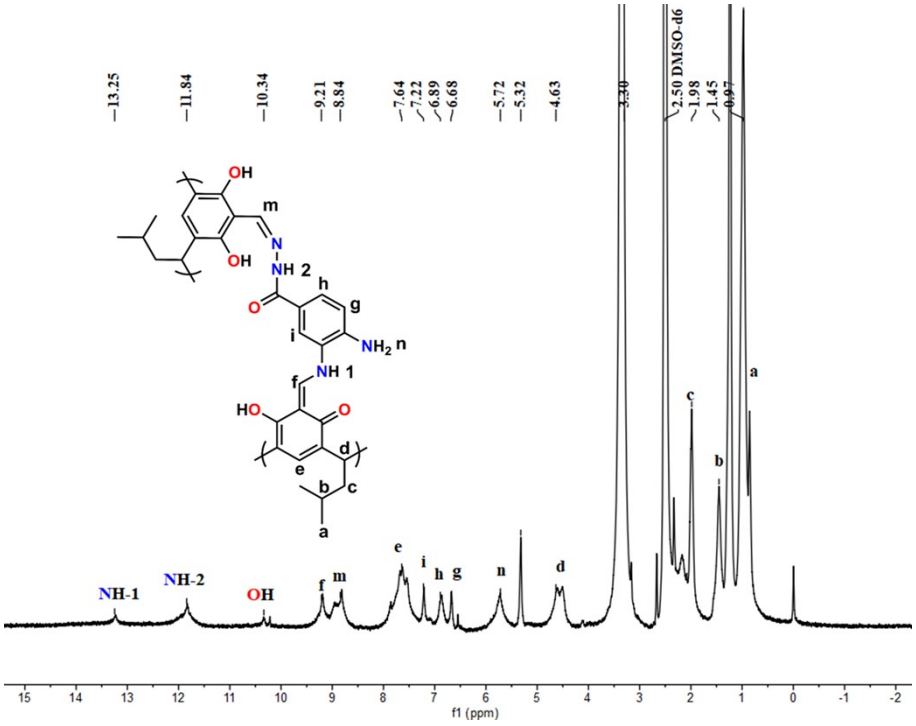

Figure S3. ^{1}H NMR spectrum of **DPOC-1.**

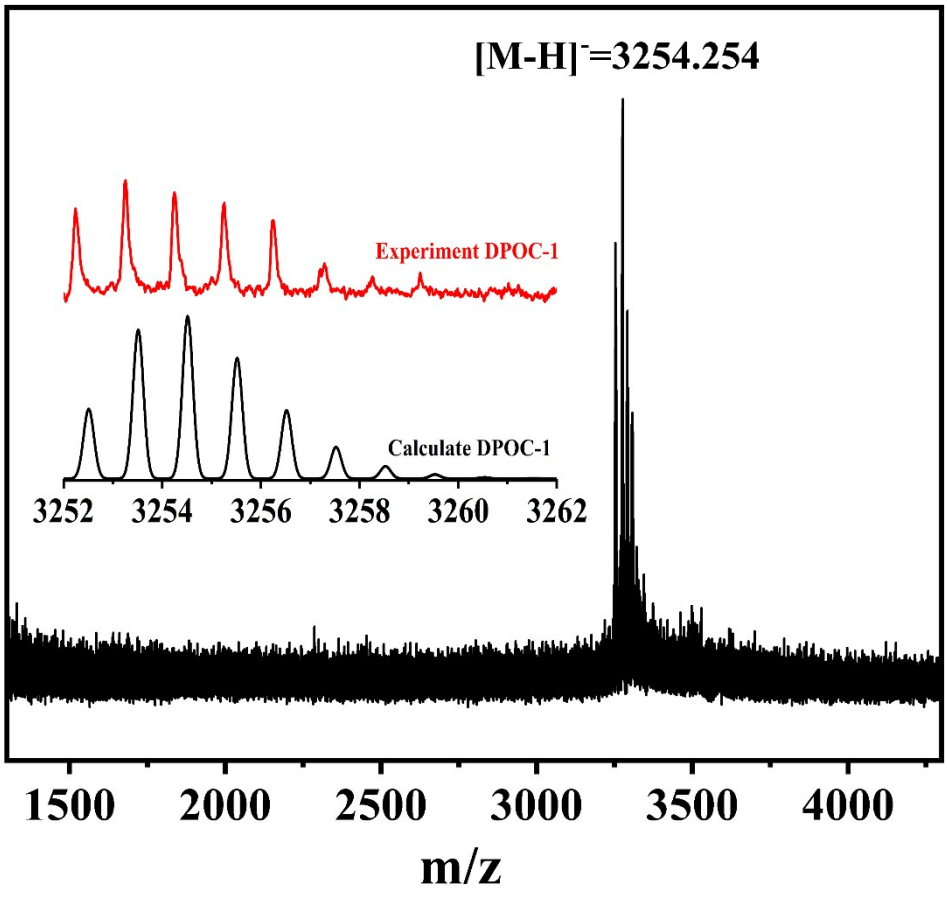

Figure S4. MALDI-TOF-MS mass spectrum of **DPOC-1** from DMF.

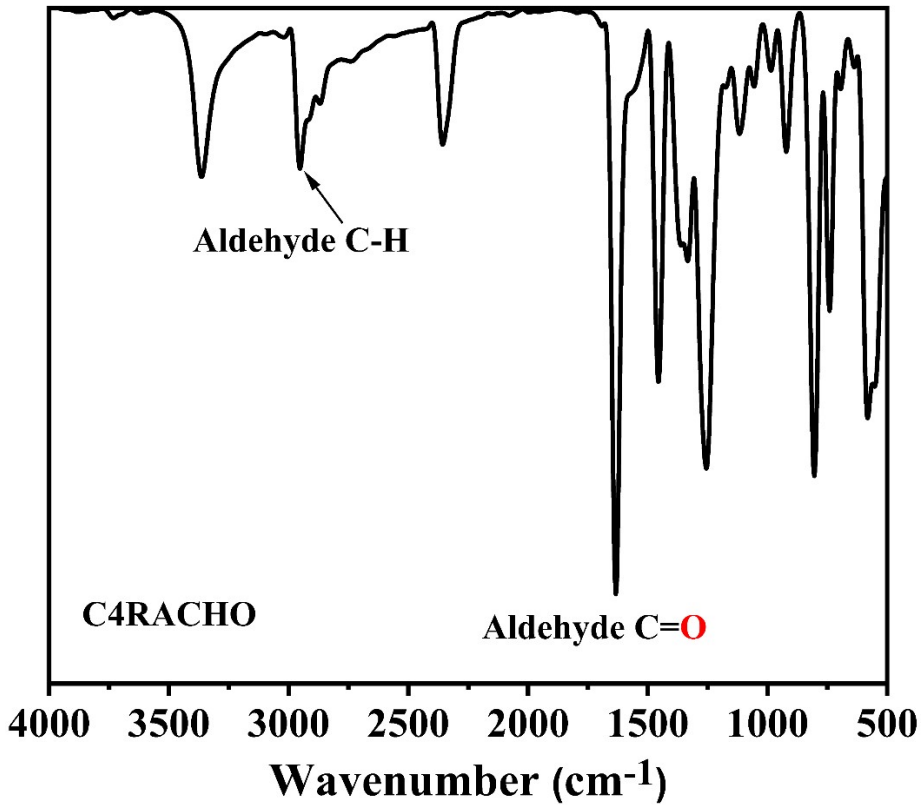

Figure S5. FT-IR spectrum of **C4RACHO**.

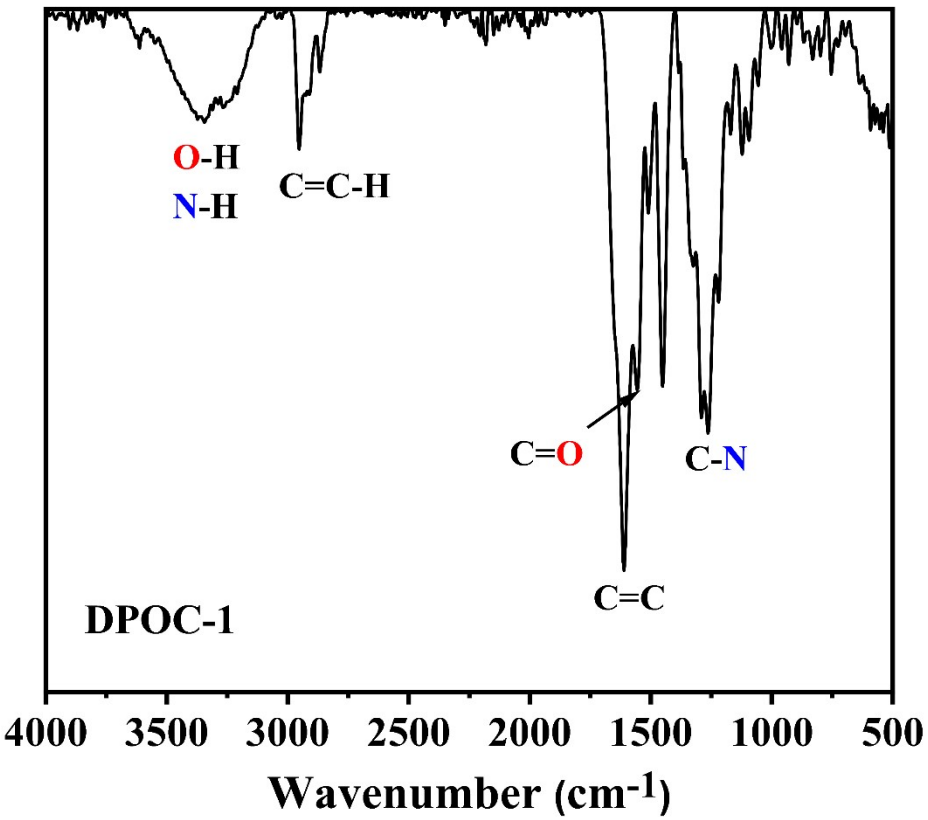

Figure S6. FT-IR spectrum of **DPOC-1**.

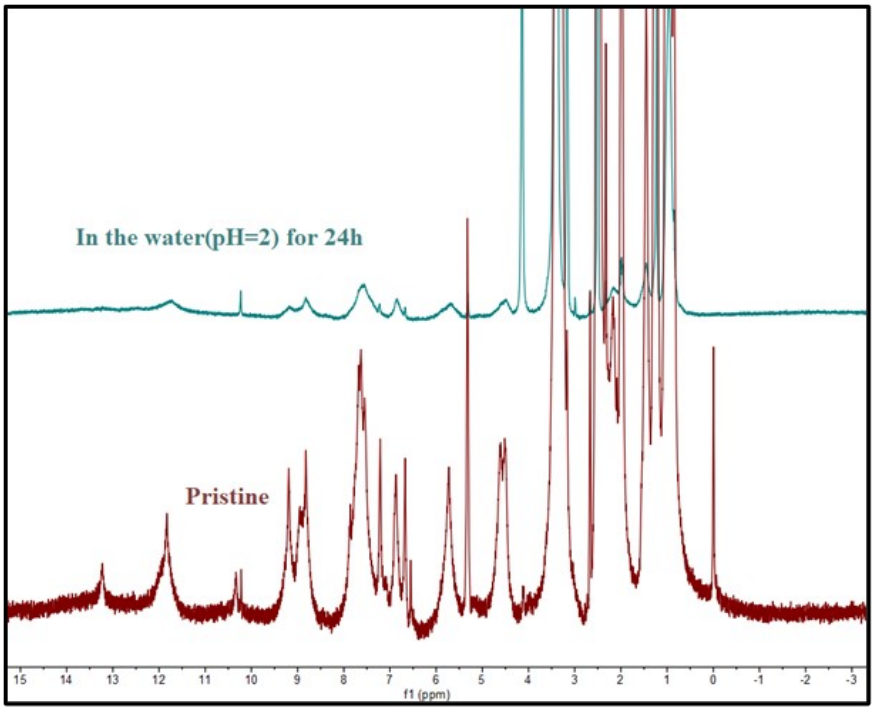

Figure S7. Comparison of ^{1}H NMR Spectra Between Fresh **DPOC-1** and **DPOC-1** Immersed in Aqueous Solutions (pH = 2).

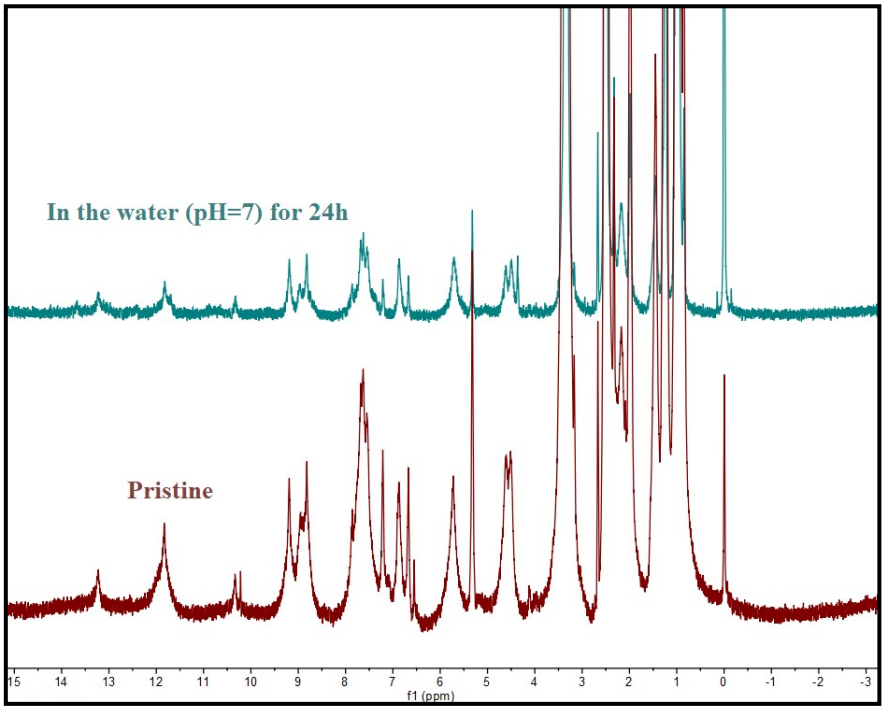

Figure S8. Comparison of ^{1}H NMR Spectra Between Fresh **DPOC-1** and **DPOC-1** Immersed in Aqueous Solutions (pH = 7).

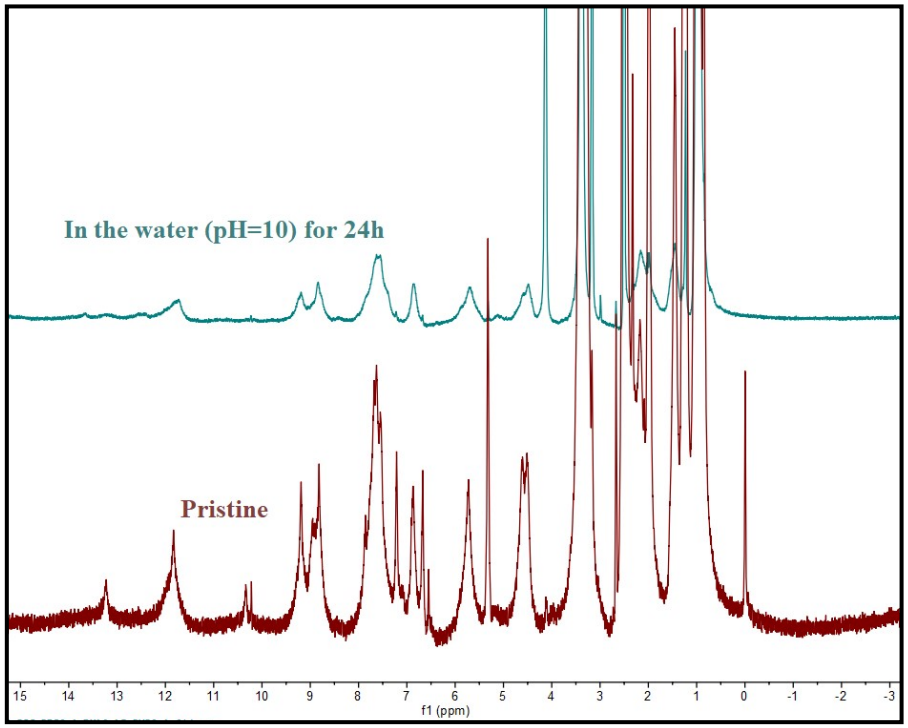

Figure S9. Comparison of ^{1}H NMR Spectra Between Fresh **DPOC-1** and **DPOC-1** Immersed in Aqueous Solutions (pH = 10).

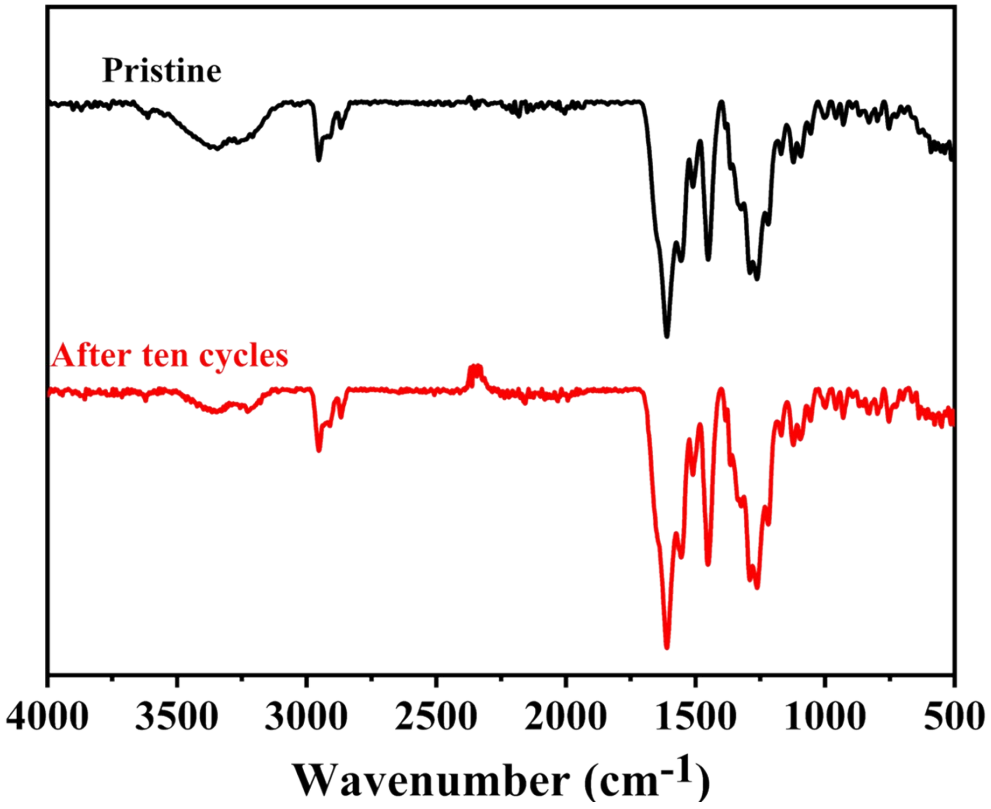

Figure S10. FT-IR spectra of **DPOC-1** before and after ten cycles.

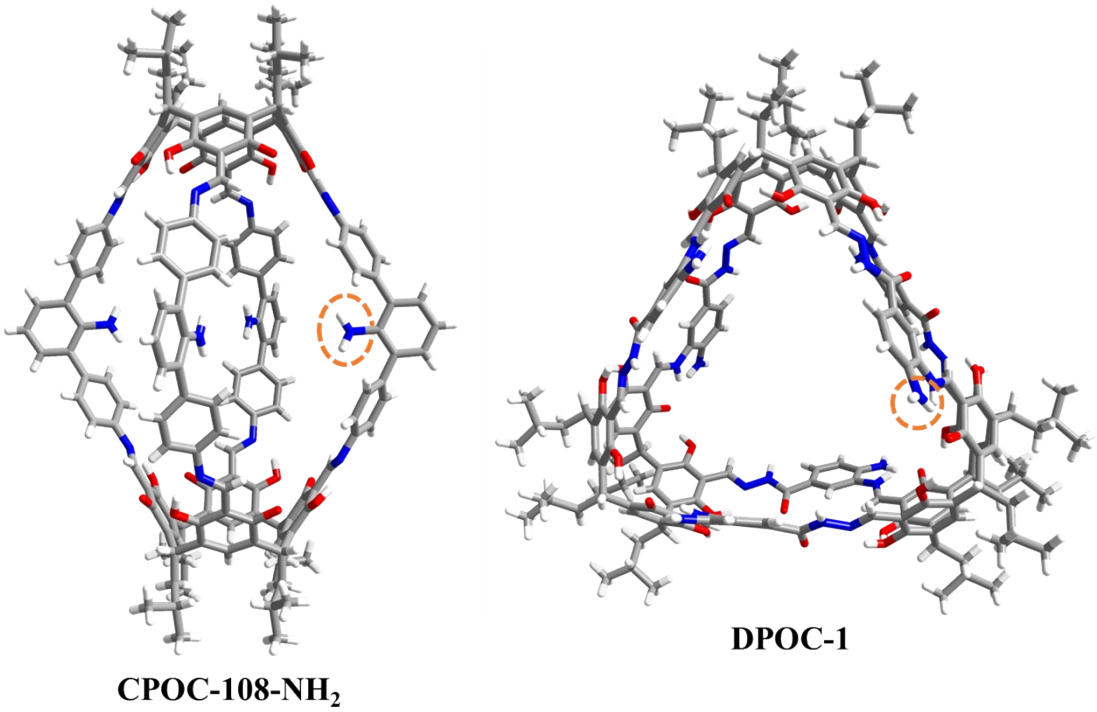

Figure S11. Schematic Diagram of Amino Functional Groups Located Within the Cage Cavity and on the Surface.

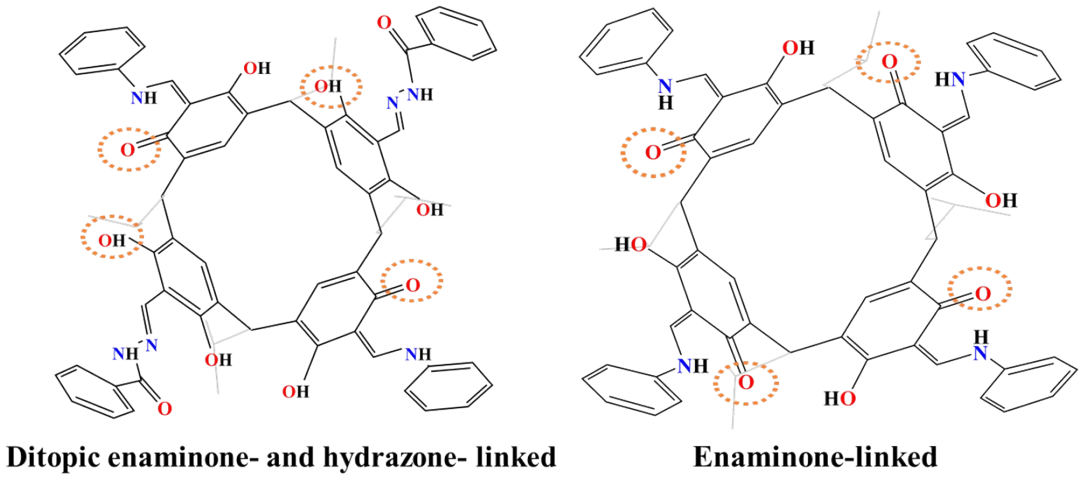

Figure S12. Structural Schematic of ditopic enaminone and hydrazone linkages (left) and enaminone linkages in C4RA-based POCs.

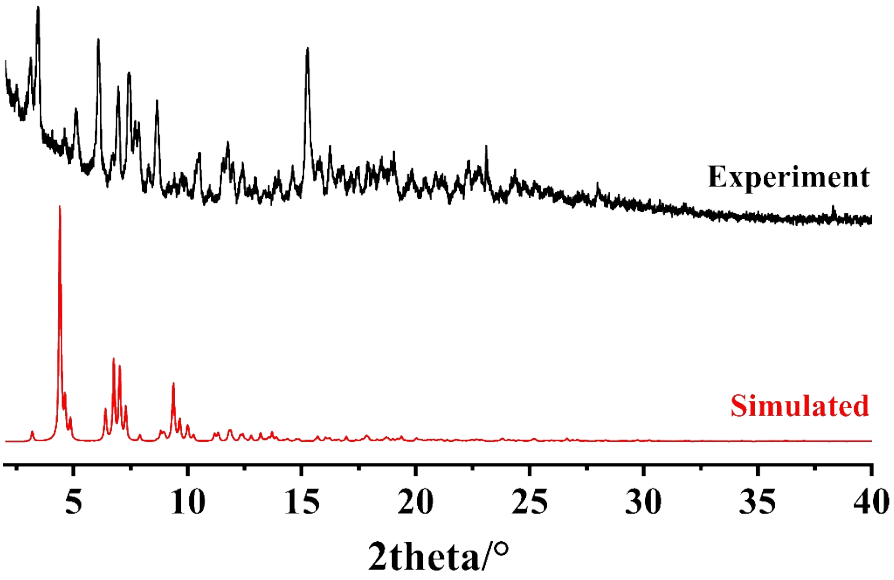

Figure S13. PXRD pattern of **DPOC-1.**

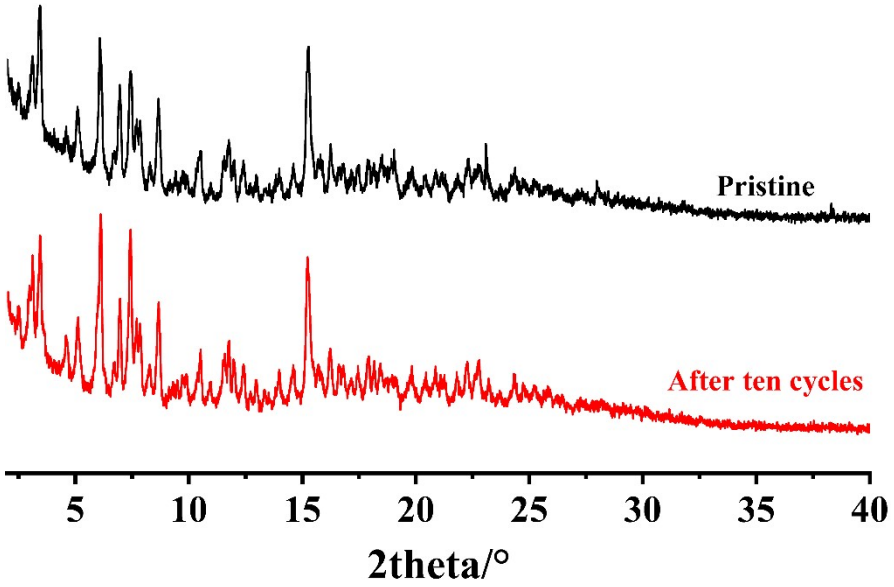

Figure S14. PXRD patterns of **DPOC-1** before and after ten cycles.

Note: PXRD analysis showed that all the experimental powder X-ray diffractograms of POC samples do not keep their original crystallinity compared to the powder X-ray diffractograms calculated from their single crystal structure data. This might be ascribed to that the packings of the isolated cage compounds are assembled by weak supramolecular interactions, which are different to MOFs and COFs assembled with much stronger coordination bonds and covalent bonds, respectively. These phenomena are often observed in cage system, especially for those with large cavities[2-4].

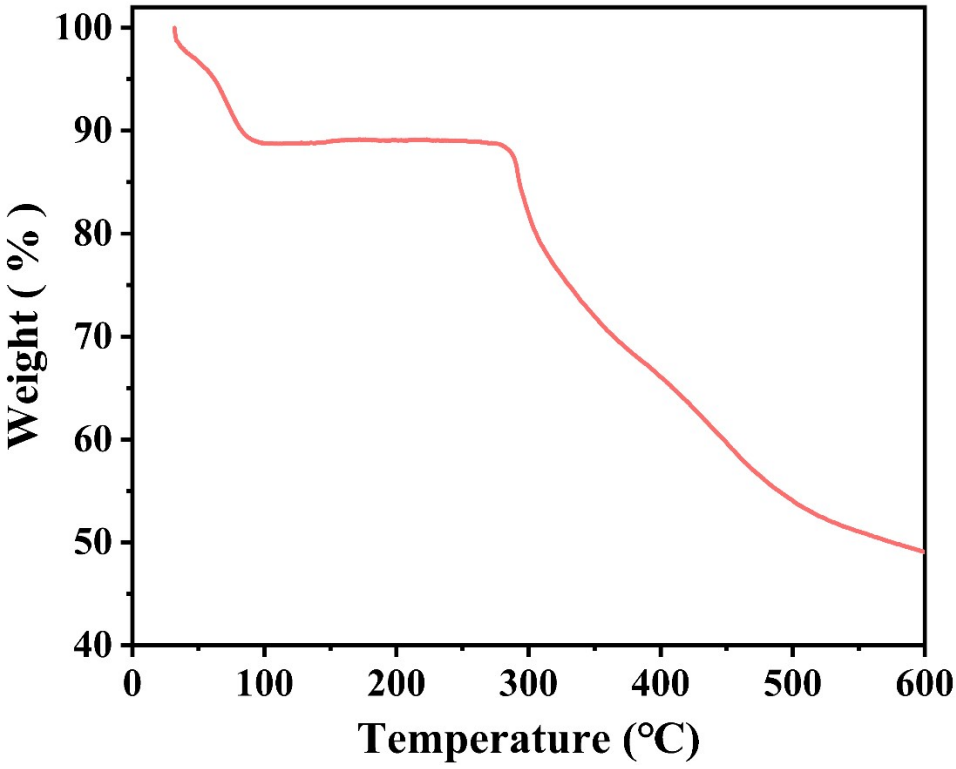

Figure S15. TGA curves of **DPOC-1.**

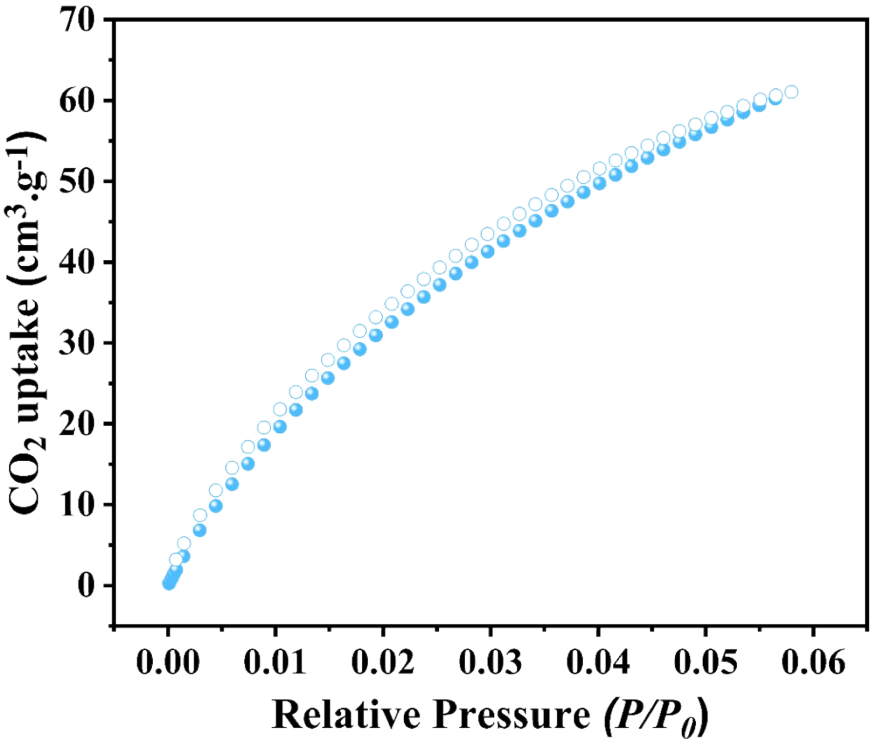

Figure S16. CO_2 gas sorption isotherms at 298K for **DPOC-1.**

Section S3. X-ray Data Collection and Structure Determination

Single-Crystal X-ray Crystallography: X-ray single crystal data for **DPOC-1** was collected on XtaLAB Synergy R, HyPix diffractometer equipped with PhotonJet R (Cu) X-ray source (λ = 1.5406 Å). The crystal structure was resolved by direct methods and all calculations were performed on the SHELXTL-2018 program package. All non-hydrogen atoms were refined anisotropically for the DPOC-1. Hydrogen atoms of the organic ligands were added in the riding model and refined with isotropic thermal parameters. Moreover, the diffuse electron density together with highly disordered solvent molecules of crystallization could not be generated and were not included for **DPOC-1**. Thus, the crystal structures were treated by the "SQUEEZE" method, a part of the PLATON package of crystallographic software. This had dramatically improved the agreement indices. Moreover, the high R_1 and wR_2 factor for **DPOC-1** might be due to the weak crystal diffraction, the disorder of the isobutyl groups as well as no heavy atoms in the molecular structure, which are typical, especially for in organic cage system[5-8]. The detail crystal data and cell parameters for **DPOC-1** are summarized in Tables S1.

Table S1. Crystallographic Data and Structure Refinement for **DPOC-1.**

	DPOC-1
Formula	$C_{186}H_{202}N_{24}O_{30}$
M / g mol^{-1}	3255.72
T / K	293(2)
Crystal system	monoclinic
Space group	I2/a
***a* / Å**	20.5106(3)
***b* / Å**	40.0760(5)
***c* / Å**	38.3715(5)
***α* (°)**	90
***β* (°)**	96.2950(10)
***γ* (°)**	90
V / Å^3	31350.5(7)
Z	4
μ (mm^{-1})	0.384
Reflections collected	108932
Ind. reflns	28023
Parameters	1093
GOF on F^2	1.503
R_1[a] [I ›σ(I)]	0.1153
wR_2[b]	0.3696
CCDC number	2490509

[a]$R_1 = \sum||F_o| - |F_c||/\sum|F_o|$. [b]$wR_2 = \{\sum[w(F_o^2 - F_c^2)^2]/\sum[w(F_o^2)^2]\}^{1/2}$

Section S4. MnO_4^- adsorption tests

Procedures for the DPOC-1 Time-Dependent Study.

DPOC-1 (10 mg) was dispersed in 5 mL of a potassium permanganate solution (25 ppm $KMnO_4$) under continuous stirring to ensure homogeneous dispersion. At designated time intervals, aliquots were withdrawn and immediately filtered through a 0.22 µm syringe filter. The residual permanganate (MnO_4^-) concentration in the filtrate was quantified by liquid-phase UV-vis spectroscopy, monitoring the characteristic absorption peaks at 525 nm and 545 nm. This allowed determination of the extent of MnO_4^- removal from the aqueous phase. Furthermore, time-dependent studies were conducted to establish: the MnO_4^- removal efficiency (%) as a function of time, the temporal concentration decay profile. The experimental kinetic data were subsequently fitted to both pseudo-first-order and pseudo-second-order kinetic models.

$$removal\ efficiency = \frac{A_0 - A_t}{A_0} \times 100\% \quad (1)$$

With A_0: The initial absorbance before adsorption. A_t: Absorbance after time t.

Adsorption kinetics study: The pseudo-first-order and pseudo-second-order models were employed to help understand the adsorption kinetics. The linear forms of the two models can be expressed by the following equation (2) and (3):

The pseudo-first order model (2)

$$Q_t = Q_e(1 - e^{-k_1 t}) \quad (2)$$

The pseudo-second order model (3)

$$\frac{t}{Q_t} = \frac{1}{k_2 \cdot Q_e^2} + \frac{t}{Q_e} \quad (3)$$

Where Q_e (mg g^{-1}) and Q_t (mg g^{-1}) refer to the adsorption capacity at equilibrium and at time t (s); k_1 (s^{-1}) and k_2 (g mg^{-1} s^{-1}) are the adsorption rate constants for the pseudo-first-order and pseudo-second-order, respectively. Qe can be calculated by the formula (4):

$$Q_t = (C_0 - C_t) \cdot \frac{v}{m} \quad (4)$$

Q_t, C_0, C_t, V and m respectively refer to, Qt: the adsorbent adsorption capacity at a specific time ($mg \cdot g^{-1}$), C_0: the initial concentration of the solution ($mg \cdot L^{-1}$), Ct: the solution concentration at a specific time ($mg \cdot L^{-1}$), V: the volume of the solution (L), m: the mass of the adsorbent (g).

Selective Adsorption Experiments. To evaluate the selectivity of DPOC-1 toward permanganate (MnO_4^-) in complex matrices, adsorption tests were conducted in the presence of common wastewater anions (Cl^-, SO_4^{2-}, $H_2PO_4^-$, Br^-). Mixed solutions were prepared with a molar ratio of competing anion to MnO_4^- (X^-:MnO_4^-) of 100:1. Specifically, 5 mL of $KMnO_4$ solution (25 ppm MnO_4^-) was introduced into 10 mL vials, followed by addition of respective potassium salts (KCl, K_2SO_4, KH_2PO_4, KBr) or their mixture (denoted MIX) to achieve the designated molar ratio. DPOC-1 (5mg) was then added to each vial. The suspensions were vortex-mixed for 30 seconds and continuously stirred for 2 hours to ensure adsorption equilibrium. Post-equilibrium, solids were removed via 0.22 μm filtration, and the resulting supernatants were analyzed by UV-vis spectroscopy (monitoring 525 and 545 nm absorbance) and inductively coupled plasma (ICP) techniques to quantify residual MnO_4^- concentrations.

PH-Dependent Adsorption Experiments. To study the performance of DPOC-1 in capturing MnO_4^- under different pH conditions in practical environments, we used dilute HCl and NaOH solutions to adjust the solution pH. Specifically: first added 5 mL of potassium permanganate solution (25 ppm MnO_4^-) to a 10 mL vial, adjusted the solution pH to 2–10,added 5 mg DPOC-1, shaken well and continuously stirred to reach adsorption equilibrium (2h), finally filtered solid particles from the solution. Measured the supernatant using liquid-phase UV-vis spectroscopy and ICP.

Calculation of Capacity. To quantify the adsorption capacity of DPOC-1, 5 mg samples were individually added to 5 mL permanganate (MnO_4^-) solutions with varying initial concentrations (20–1000 ppm). Each mixture was stirred for a fixed duration (2h) to achieve adsorption equilibrium. The adsorption capacity was calculated using the following formula based on UV-vis absorbance measurements of initial and equilibrated solutions，

$$Q_e = (C_0 - C_t) \cdot \frac{v}{m} \quad (5)$$

Q_t, C_0, C_t, V and m respectively refer to, Q_e: equilibrium adsorption capacity ($mg \cdot g^{-1}$), C_0: the initial concentration of the solution ($mg \cdot L^{-1}$), C_t: the solution concentration at a specific time ($mg \cdot L^{-1}$), V: the volume of the solution (L), m: the mass of the adsorbent (g).

Adsorbent Recyclability Testing. The adsorbed DPOC-1 was regenerated via simple methanol immersion. The regenerated material was then added to 5 mL of permanganate solution (25 ppm MnO_4^-) for five consecutive adsorption cycles. Experimental results were recorded using liquid-phase UV-vis spectroscopy at each cycle.

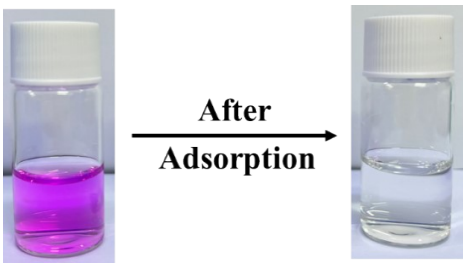

Figure S17. The optical image of the MnO_4^- solution before and after removal by **DPOC-1.**

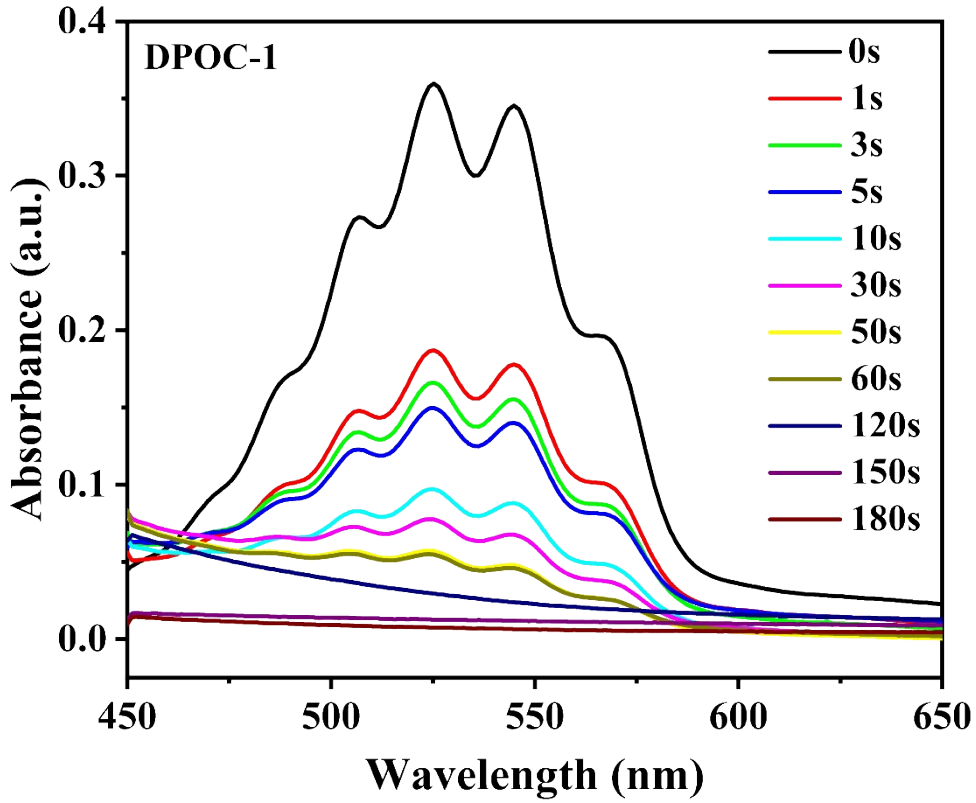

Figure S18. Time-dependent UV–Vis spectra upon the addition of **DPOC-1.**

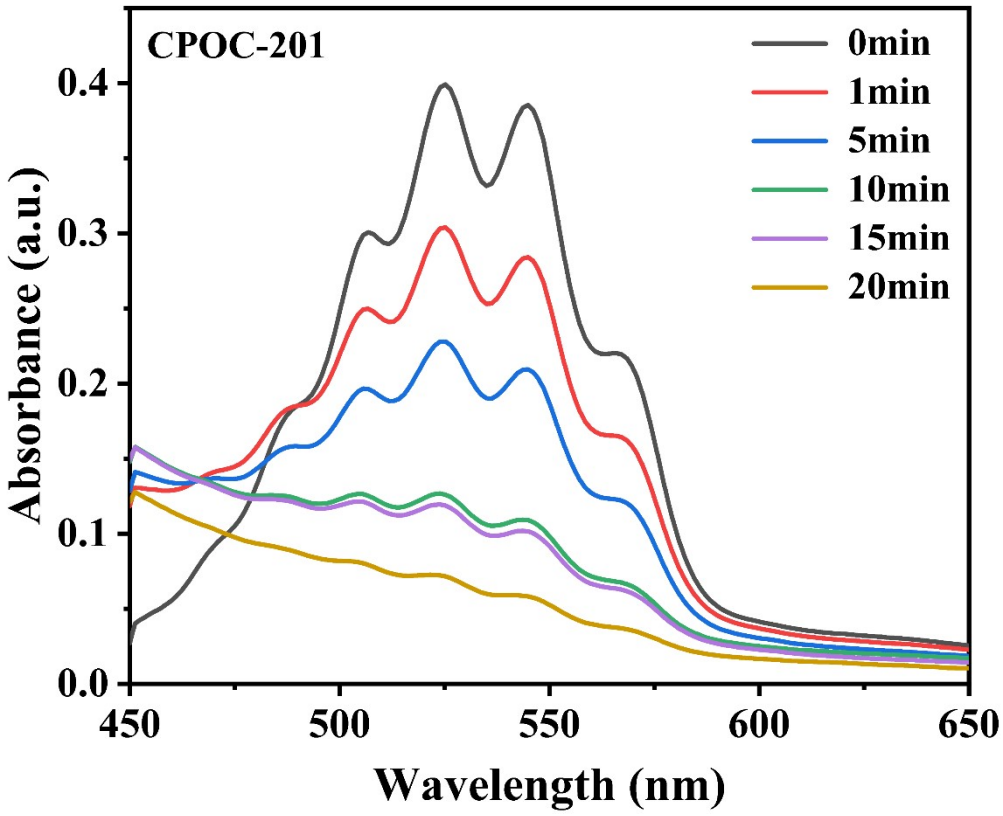

Figure S19. Time-dependent UV–Vis spectra upon the addition of **CPOC-201.**

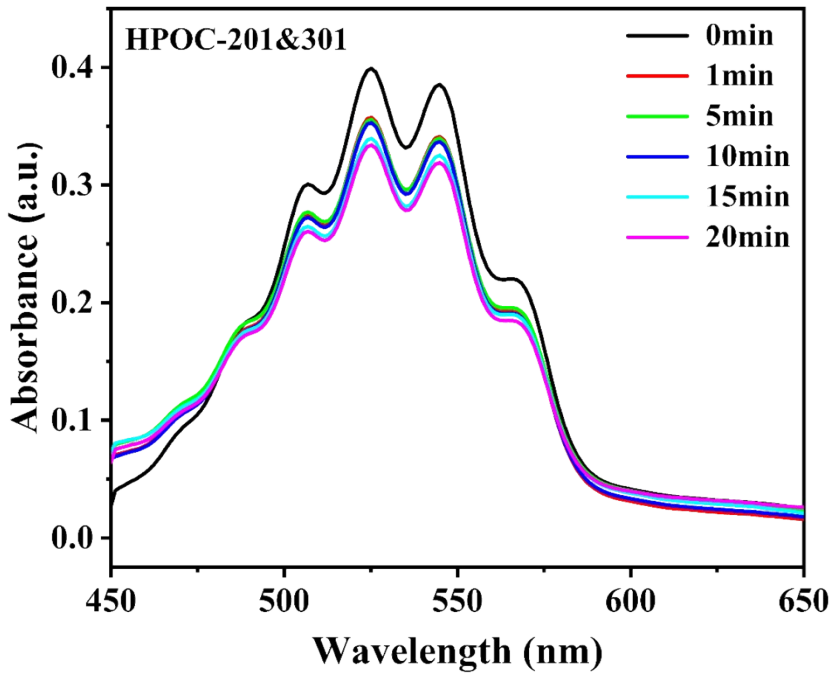

Figure S20. Time-dependent UV–Vis spectra upon the addition of **HPOC-201&301.**

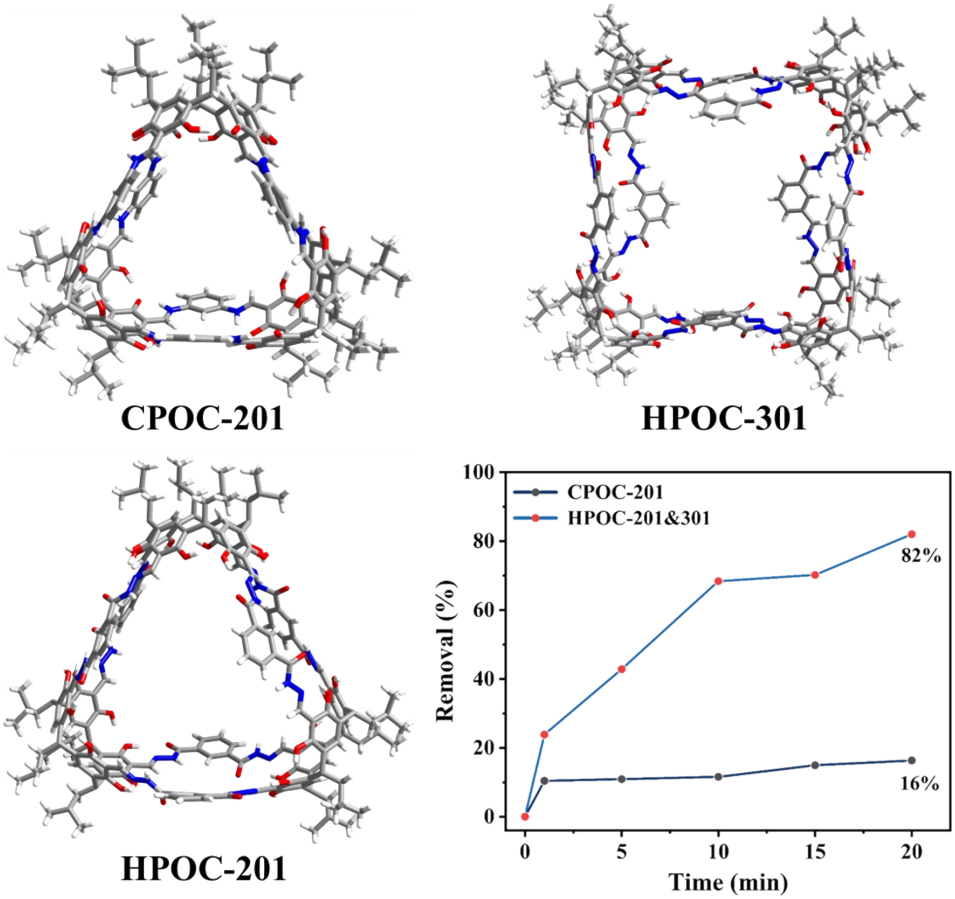

Figure S21. SCXRD structures for **HPOC-301**, **HPOC-301** and **CPOC-201**; the MnO_4^- adsorption removal efficiency of **CPOC-201** and **HPOC-201&301** is based on the absorption peak at 525 nm.

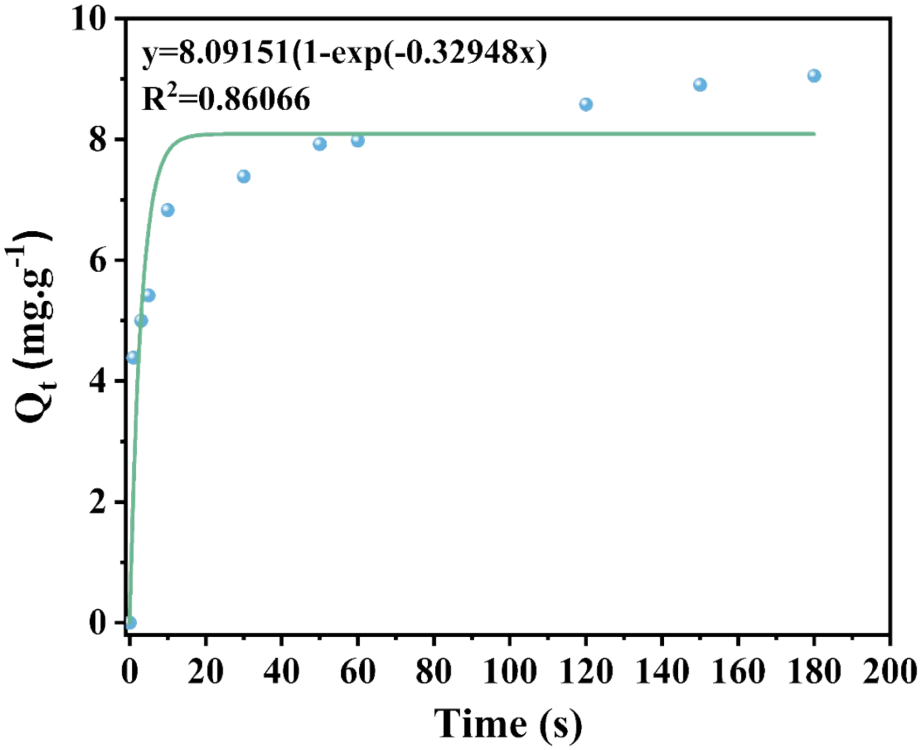

Figure S22. Pseudo-first-order model for the adsorption of MnO_4^- by **DPOC-1**.

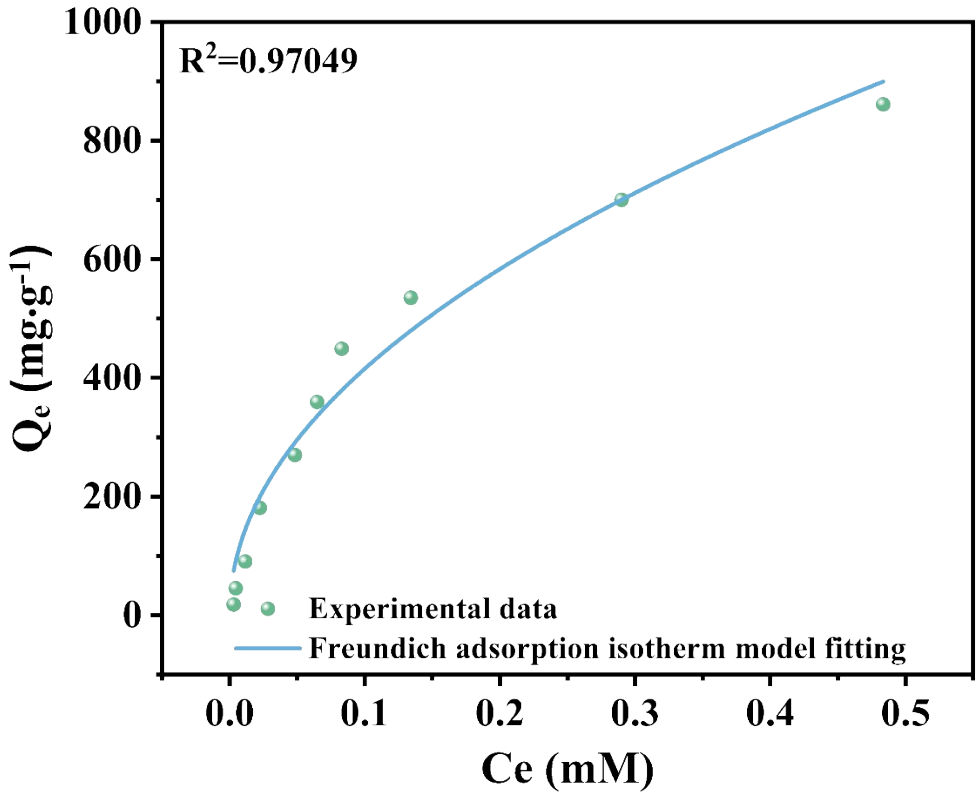

Figure S23. Freundich model for the adsorption of MnO_4^- by **DPOC-1**.

Table S2. Kinetic data of **DPOC-1** for the adsorption of MnO_4^- ions.

t (s)	C_t (mg.L^{-1})	Q_t (mg.g^{-1})
0	18.46	0
1	9.68	4.388
3	8.46	4.999
5	7.62	5.418
10	4.79	6.831
30	3.68	7.389
50	2.61	7.923
60	2.50	7.979
120	1.29	8.582
150	0.65	8.905
180	0.35	9.054

Table S3. Thermodynamic data of **DPOC-1** for the adsorption of MnO_4^- ions.

C_0 (mg.L^{-1})	C_e (mg.L^{-1})	Q_e (mg.g^{-1})
18.37	0.36	18.006
45.92	0.55	45.369
91.84	1.37	90.460
183.68	2.66	181.013
275.52	5.74	269.771
367.36	7.70	359.653
459.20	9.86	449.338
551.04	15.95	535.085
734.72	34.49	700.227
918.40	57.50	860.896

Table S4. Kinetic parameters of MnO_4^- in aqueous solution into **DPOC-1.**

Adsorbent	Model	Parameters	
DPOC-1	Pseudo-first-order	Q_e（mg g^{-1}）	8.092
		k_1(s^{-1})	0.3295
		R^2	0.86066
	Pseudo-second-order	Q_e（mg g^{-1}）	9.109
		k_2(s^{-1})	0.0243
		R^2	0.99799

Table S5. Thermodynamic parameters of MnO_4^- in aqueous solution into **DPOC-1.**

Adsorbent	Model	Parameters	
DPOC-1	Langmuir model	Q_{max}（mg g^{-1}）	1145
		K	7.35
		R^2	0.994
	Freundlich Model	K_f	1341
		1/n	0.49
		R^2	0.970

Table S6. A comparison table of MnO_4^- capture (mg/g) with some well-studied examples in

the literature (ND-Not done).

Compound	Capacity(mg/g)	Selectivity	Reference
DPOC-1	**1145**	**Br^-, $H_2PO_4^-$, SO_4^{2-}, Cl^-**	**This work**
Ox-FVESP	1428.57	ND	9
$[Cu_3Cl(L)(H_2O)_2]\cdot Cl\cdot 4DMA\cdot 8H_2O$	106	ClO_4^-,NO_3^-,PF_6^-, $H_2PO_4^-$	10
ZrIT-1	276.6	ClO_4^-, NO_3^-, $H_2PO_4^-$, SO_4^{2-}, BF_4^-	11
SLUG-21	283	NO_3^-, CO_3^{2-}	12
iPOP-ANT	5372	Cl^-, Br^-, NO_3^-	13
SCNU-Z1-Cl	313.5	Cl^-, ClO_4^-, NO_3^- N_3^-, SO_4^{2-}	14
Compound-1	297.3	Cl^-, Br^-, NO_3^-, SO_4^{2-}	15
$Ag(btr)\cdot PF_6\cdot 0.5CH_3CN$	163	NO_3^-, BF_4^-, ClO_4^-	16
QUST-iPOP-1	514.86	Cl^-, Br^-, NO_3^-, SO_4^{2-}	17

Section S5: Computational Details for Host–Guest Complex Optimization

Initial Structure Generation

The initial binding configurations of the permanganate anion (MnO_4^-) within the organic molecular cage were identified using a hierarchical screening protocol. First, a global conformational search was performed using the AutoDock Vina docking program. The molecular cage was treated as a rigid receptor, while the MnO_4^- ion was treated as a flexible ligand to explore its translational and rotational degrees of freedom within the cage cavity. A search box encompassing the entire internal void of the cage was defined to ensure exhaustive sampling. The top-ranking docking poses, characterized by the most favorable empirical binding scores, were selected as initial guesses for subsequent high-level quantum mechanical optimizations.

DFT Geometry Optimization and Energy Calculations

All selected host–guest complexes were fully optimized using density functional theory (DFT) as implemented in the CP2K software package (version 2026.1). The electronic structure was described using the PBE-D4 exchange-correlation functional, which includes empirical dispersion corrections to accurately capture the non-covalent interactions (e.g., van der Waals forces, pi-anion interactions) governing the host–guest binding.

The Kohn–Sham orbitals were expanded in a Gaussian and Plane Waves (GPW) dual basis set approach. Specifically, the molecular orbitals were represented using the DZVP-MOLOPT-SR-GTH basis set, while the electron density was expanded in an auxiliary plane wave basis set with a kinetic energy cutoff of 400 Ry. Goedecker–Teter–Hutter (GTH) pseudopotentials were employed to describe the core electrons, treating the valence electrons explicitly.

Binding Energy Calculation

The binding energy (ΔE_{bind}) of the MnO_4^-@Cage complex was calculated as the energy difference between the optimized complex and the isolated components:

$$\Delta E_{bind} = E_{complex} - (E_{cage} + E_{MnO4-})$$

where $E_{complex}$ is the total energy of the optimized host–guest system, E_{cage} is the energy of the isolated cage (the same geometry as in the complex), and E_{MnO4-} is the energy of the isolated permanganate anion.

Table S7. Binding Energy Calculation Results.

Cage-MnO_4^-	Cage	MnO_4^-	ΔE (Ha)	ΔE (kJ/mol)
-2067.9804	-1899.635473	-168.298914	-0.046044786	-120.8905862

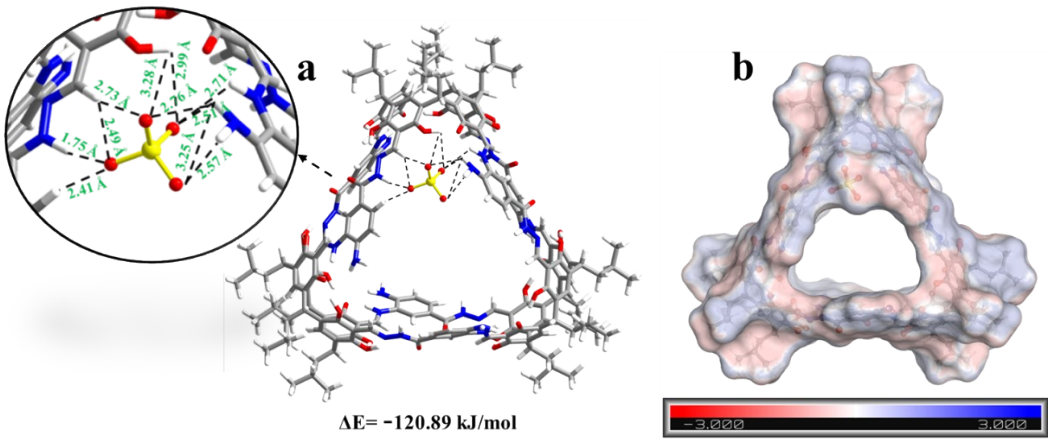

Figure S24. (a) Hydrogen bonds and sorption enthalpies; (b) Electrostatic potential (ESP) distribution map of the **DPOC-1 and MnO_4^- complex**.

References:

1. M. Grajda, M. Wierzbicki, P. Cmoch and A. Szumna, *J. Org. Chem.*, 2013, **78**, 11597-11601.
2. P. Wagner, F. Rominger, W.-S. Zhang, J. H. Gross, S. M. Elbert, R. R. Schroeder and M. Mastalerz, *Angew. Chem. Int. Ed.*, 2021, **60**, 8896-8904.
3. D. Beaudoin, F. Rominger and M. Mastalerz, *Angew. Chem. Int. Ed.*, 2017, **56**, 1244-1248.
4. S. Hong, M. R. Rohman, J. Jia, Y. Kim, D. Moon, Y. Kim, Y. H. Ko, E. Lee and K. Kim, *Angew. Chem. Int. Ed.*, 2015, **54**, 13241-13244.
5. S. Ivanova, E. Koester, J. J. Holstein, N. Keller, G. H. Clever, T. Bein and F. Beuerle, *Angew. Chem. Int. Ed.*, 2021, **60**, 17455-17463.
6. M. Yang, F. Qiu, E.-S. M. El-Sayed, W. Wang, S. Du, K. Su and D. Yuan, *Chem. Sci.*, 2021, **12**, 13307-13315.
7. S. Hong, M. R. Rohman, J. Jia, Y. Kim, D. Moon, Y. H. Ko, E. Lee and K. Kim, *Angew. Chem. Int. Ed.*, 2015, **54**, 13241-13244.
8. J. Koo, I. Kim, Y. Kim, D. Cho, I.-C. Hwang, R. D. Mukhopadhyay, H. Song, Y. H. Ko, A. Dhamija, H. Lee, W. Hwang, S. Kim, M.-H. Baik and K. Kim, *Chem*, 2020, **6**, 3374-3384.
9. S. A. Bani-Atta, *Sci. Rep.*, 2022, **12**, 4547.
10. Y. Li, J. Yang and J.-F. Ma, *Dalton Trans.*, 2021, **50**, 3832-3840.
11. B. Hou, X. Gu, H. Gan, H. Zheng, Y. Zhu, X. Wang and Z. Su, *Inorg. Chem.*, 2022, **61**, 7103-7110.
12. D. L. R. Honghan Fei, and Scott R. J. Oliver*, *J. Am. Chem. Soc.*, 2010, **132**, 7202–7209.
13. S. Sarkar, A. Chakraborty, R. Ranjan, P. Nag, S. R. Vennapusa and S. Mukhopadhyay, *Mater. Chem. Front.*, 2022, **6**, 3070-3083.
14. S.-Q. Deng, X.-J. Mo, S.-R. Zheng, X. Jin, Y. Gao, S.-L. Cai, J. Fan and W.-G. Zhang, *Inorg. Chem.*, 2019, **58**, 2899-2909.
15. P. Samanta, P. Chandra, S. Dutta, Aamod V. Desai and S. K. Ghosh, *Chem. Sci.*, 2018, **9**, 7874-7881.
16. X. Li, Y. Gong, H. Zhao and R. Wang, *Inorg. Chem.*, 2014, **53**, 12127-12134.
17. S. Jiao, L. Deng, X. Zhang, Y. Zhang, K. Liu, S. Li, L. Wang and D. Ma, *ACS Appl Mater Interfaces*, 2021, **13**, 39404-39413.